Validation of Lagrangian two-way coupled point-particle models in large-eddy simulations

K. Fröhlich ·
L. Schneiders · M. Meinke · W. Schröder

Abstract The accuracy of point-particle models with two-way coupling for particles of Kolmogorov-length-scale size is assessed. Turbulent kinetic energy budgets are analyzed in physical and in spectral space. It is shown that the force projection of the two-way coupling consistently models the direct transfer of kinetic energy on the particle surfaces and the enhanced viscous dissipation in the vicinity of the particles. Direct and large-eddy simulations of particle-laden flows in isotropic decaying turbulence are conducted and compared with direct-particle fluid simulations, where the particle-fluid interaction is fully resolved. An analysis in spectral space shows that turbulence modulation by particles mainly occurs at larger scales, although the momentum transfer takes place at the smallest scales. Therefore, the turbulent kinetic energy cascade of the single phase dominates in particle-laden flows. It is shown that point-particle models do not interfere with subgrid scale models, which usually act on the smallest scale. Consequently, point-particle models predict sufficiently accurate the turbulence modulation in direct numerical simulations and even when a subgrid scale model is used. The resolution of the LES does not affect the accuracy of the point-particle model, when the subgrid kinetic energy is negligible.

K. Fröhlich · L. Schneiders
Institute of Aerodynamics, RWTH Aachen University, Aachen, Germany,
Wüllnerstr. 5a, 52062 Aachen, Germany
E-mail: k.froehlich@aia.rwth-aachen.de
E-mail: l.schneiders@aia.rwth-aachen.de

M. Meinke · W. Schröder
Institute of Aerodynamics, RWTH Aachen University, Aachen, Germany,
Wüllnerstr. 5a, 52062 Aachen, Germany
Jülich Aachen Research Alliance - High Performace Computing
E-mail: m.meinke@aia.rwth-aachen.de
E-mail: office@aia.rwth-aachen.de

1 Introduction

Particle-laden turbulent flow is of importance in a broad field of applications including natural and technical environments. Examples may be found in the settling of aerosol particles in atmospheric flows, in the transport of dust through the human respiration system, in fuel injections of internal combustion engines, as well as in the combustion of pulverized coal particles in a furnace. Due to the numerous scales involved, particle-laden flow reveals complex interaction phenomena such as turbulence modulation. The formulation of two-way coupled Lagrangian point-particle models, where the impact of the particles on the turbulent flow is projected into the governing equations of the flow field, is still controversially discussed and no universal method is defined, yet. The quality of several realizations of point-particle models has been compared in [18], which have been used ,e.g., in [49, 15, 51, 7], without any conclusive recommendation. Extensions on two-way coupled point-particle models (PPMs) have been proposed in [23, 25, 26], which mainly focus on an accurate computation of the Stokes drag acting on the particle when using a two-way coupled approach. However, for particle diameters d_p larger than the Kolmogorov scale η, a justification for the validity of a force projection is still missing. Several studies have been performed to assess the accuracy of PPMs for a single finite-sized particle in isotropic and anisotropic turbulent flow fields [4, 5, 59, 9]. It has been consistently observed that the mean value of the overall forces acting on the particle is correctly predicted by the Stokesian drag law, while the rms-values of the force may be significantly different due to the rapid flow scales which are smaller than the particles. The analysis of a single particle is nevertheless not suited to provide information about the quality of two-way coupled PPMs.

Additional modeling is required, if PPMs are applied in large-eddy simulations (LES). Several models, e.g., stochastic models [19, 48], approximate deconvolution [30, 28], and a combination of both [38], have been proposed in previous studies for one-way coupling problems to recover portions of subgrid turbulent kinetic energy. Significantly less studies are available on two-way coupled point-particle LES. An analysis has been performed in [8] for different subgrid scale (sgs) turbulence models. The focus was on a priori tests, where the flow field of a direct numerical simulation (DNS) has been used for the particle-fluid coupling, and filtered afterwards. A better understanding of two-way coupling in LES is necessary [29]. A thorough assessment of two-way coupling in LES including a comparison with fully-resolved particle-laden flows is still missing since detailed reference data hardly exist. Simulations involving $\mathcal{O}(1000)$ particles with $d_p \sim \eta$ are necessary to perform a severe validation of PPMs. Recently, direct-particle fluid simulations (DPFS) have been performed in [46, 45], in which all particle and fluid scales are fully resolved. In [46], $45,000$ spherical and ellipsoidal particles with $d_p \sim \eta$ and a particle-to-fluid density ratio $\rho_p/\rho = 1400$ have been analyzed in isotropic decaying turbulence and directly compared with a two-way coupled PPM. It has been shown that PPMs correctly predict the turbulence modulation for spherical particles, but do not resolve the viscous dissipation rate, which is induced by the particles. This particle induced dissipation has been quantified in [45]. By analyzing $45,000$ particles with $d_p \sim \eta$ and density ratios ranging from $\rho_p/\rho = 40$ to 5000, an analytical expression has been derived, which can be used to evaluate PPMs. By considering energy budgets, it has been shown that the

two-way coupled PPM implicitly contains the particle induced dissipation, which will be extended to the spectral space.

The purpose of the present study is to utilize the results and the reference data compiled in [45] to assess the accuracy of two-way coupled PPMs in DNS and LES. Therefore, the isotropic decaying turbulent flow from [45] with the initial Taylor-scale Reynolds number $Re_\lambda = 79$ defines the background flow field and four density ratios are considered. Particle-laden DNS and three resolutions of LES using two-way coupled PPM are performed and the results are compared with the DPFS. The goal of this study is to provide answers to the following questions:

– Are two-way coupled PPMs appropriate to capture the turbulence modulation by particles of Kolmogorov-length-scale size?
– Are single phase sgs models suited for particle-laden flows and how do PPMs interact with sgs models?
– Does the resolution of the LES affect the accuracy of PPMs?

After introducing the underlying mathematical models of the flow field and the particle dynamics in Sec. 2, the monotone implicit LES (MILES) approach is presented in Sec. 3, where the numerical scheme provides an implicit sgs model. Subsequently, it will be shown in Sec. 4 that the single phase LES of the isotropic turbulence shows good agreement with the DNS. Next, a consistent comparison with the reference data of [45] will be presented by considering turbulent kinetic energy budgets in physical space. Concluding remarks are given in Sec. 5.

2 Mathematical models

In this section, the compressible Navier-Stokes equations in integral formulation are introduced. Subsequently, analytical kinematic and dynamic equations for the particle phase are formulated.

2.1 Fluid phase equations

The conservation of mass, momentum, and energy in a control volume V may be expressed in integral form by

$$\int_V \frac{\partial \boldsymbol{Q}}{\partial t}\, dV + \int_{\partial V} \bar{\boldsymbol{H}} \cdot \boldsymbol{n}\, dA = \boldsymbol{0},$$ (1)

where $\boldsymbol{Q} = [\ \rho_f,\ \rho_f \boldsymbol{u}^T,\ \rho_f E\ ]^T$ is the vector of conservative Eulerian variables and $\bar{\boldsymbol{H}}$ is the flux tensor through the surface ∂V of V in outward normal direction $\boldsymbol{n}$. The conservative variables are defined by the fluid density ρ_f, the vector of velocities $\boldsymbol{u}$, and the total specific energy $E = e + |\boldsymbol{u}|^2/2$ containing the specific internal energy e. It is useful for the development of numerical schemes to divide $\bar{\boldsymbol{H}}$ into an inviscid advection part $\bar{\boldsymbol{H}}_{inv}$ and a viscous diffusion part $\bar{\boldsymbol{H}}_{visc}$, where

$$\bar{\boldsymbol{H}} = \bar{\boldsymbol{H}}_{inv} + \bar{\boldsymbol{H}}_{visc} = \begin{pmatrix} \rho_f \boldsymbol{u} \\ \rho_f \boldsymbol{u}\boldsymbol{u} + p \\ \boldsymbol{u}\left(\rho_f E + p\right) \end{pmatrix} - \frac{1}{Re}\begin{pmatrix} \boldsymbol{0} \\ \bar{\boldsymbol{\tau}} \\ \bar{\boldsymbol{\tau}}\boldsymbol{u} - \boldsymbol{q} \end{pmatrix},$$ (2)

with the pressure p, the stress tensor $\bar{\bar{\tau}}$, the vector of heat conduction $\boldsymbol{q}$, and the Reynolds number Re. The latter is determined by $Re = \rho_\infty u_\infty L_\infty / \mu_\infty$, given the reference quantities of the density ρ_∞, the velocity u_∞, the length L_∞, and the dynamic viscosity μ_∞. Using Stokes' hypothesis for a Newtonian fluid yields an equation for the stress tensor

$$\bar{\bar{\tau}} = 2\mu\bar{\bar{S}} - \frac{2}{3}\mu\left(\boldsymbol{\nabla}\cdot\boldsymbol{u}\right)\bar{\bar{I}}, \tag{3}$$

in which $\bar{\bar{I}}$ is the unit tensor and $\bar{\bar{S}}$ holds the rate-of-strain tensor defined as $\bar{\bar{S}} = \left(\boldsymbol{\nabla}\boldsymbol{u} + \left(\boldsymbol{\nabla}\boldsymbol{u}\right)^T\right)/2$. The dynamic viscosity μ depends on the local thermodynamic state of the fluid. However, it can be approximately obtained by Sutherland's law

$$\mu\left(T\right) = \mu_\infty \left(\frac{T}{T_\infty}\right)^{3/2} \frac{T_\infty + S}{T + S}, \tag{4}$$

with S being the Sutherland temperature. Fourier's law gives the heat conduction

$$\boldsymbol{q} = -\frac{\mu}{Pr\left(\gamma - 1\right)}\boldsymbol{\nabla}T, \tag{5}$$

using the static temperature T, the constant capacity ratio $\gamma = c_p/c_v$, the specific heat capacities c_v and c_p at constant volume and at constant pressure. The Prandtl number Pr is given by $Pr = \mu_\infty c_p / k_T$ containing the thermal conductivity k_T. The system of equations can be closed by the caloric state equation $e = c_v T$ and the state equation of an ideal gas $p = \rho R T$, with R being the specific gas constant.

2.2 Particle phase equations

The acceleration of a rigid particle with constant mass under the influence of a force is given by

$$m_p \frac{d\boldsymbol{v}_p}{dt} = \boldsymbol{F}_p, \tag{6}$$

with the particle mass m_p, the particle velocity $\boldsymbol{v}_p$, and the force acting on the particle $\boldsymbol{F}_p$. Provided that the latter can be determined, the linear particle dynamics are fully closed by the kinematic relation

$$\frac{d\boldsymbol{x}_p}{dt} = \boldsymbol{v}_p, \tag{7}$$

where $\boldsymbol{x}_p$ denotes the position of the particle center of mass. The equation for rotational dynamics in a rotating frame of reference $(\tilde{x}, \tilde{y}, \tilde{z})$ reads

$$\widetilde{\bar{\bar{I}}}\frac{d\widetilde{\boldsymbol{\omega}_{\mathrm{p}}}}{dt} + \widetilde{\boldsymbol{\omega}}_{\mathrm{p}} \times \left(\widetilde{\bar{\bar{I}}}\widetilde{\boldsymbol{\omega}}_{\mathrm{p}}\right) = \widetilde{\boldsymbol{T}_p}, \tag{8}$$

where $\widetilde{\bar{\bar{I}}}$ denotes the principal moments of inertia, $\widetilde{\boldsymbol{\omega}}_p$ the angular velocity, and $\widetilde{\boldsymbol{T}}_p$ the torque acting on the particle. The rotational kinematics can be resolved using quaternions, as described in [46]. At the particle surface Γ_p, the no-slip condition is established by

$$\boldsymbol{u} = \boldsymbol{v}_p + \boldsymbol{\omega}_p \times \left(\boldsymbol{x} - \boldsymbol{r}_p\right). \tag{9}$$

Evaluating the momentum balance given by Eq. 1 at the particle surface yields the force acting on the particle $\boldsymbol{F}_p$ due to fluid pressure and fluid shear forces

$$\boldsymbol{F}_p = \oint_{\Gamma_p} \left(-p\boldsymbol{n} + \bar{\boldsymbol{\tau}} \cdot \boldsymbol{n} \right) dA. \tag{10}$$

Likewise, the torque $\boldsymbol{T}_p$ acting on the particle is computed by

$$\boldsymbol{T}_{\mathrm{p}} = \oint_{\Gamma_p} \left(\boldsymbol{x} - \boldsymbol{x}_p \right) \times \left(-p\boldsymbol{n} + \bar{\boldsymbol{\tau}} \cdot \boldsymbol{n} \right) dA, \tag{11}$$

with $\boldsymbol{x}_p$ the center of mass of the particle. The direct transport of kinetic energy between a particle and the flow field can be directly obtained with

$$\psi_p = \oint_{\Gamma_p} \left(p\boldsymbol{n} - \bar{\boldsymbol{\tau}} \cdot \boldsymbol{n} \right) \cdot \boldsymbol{u} dA = - \left(\boldsymbol{F}_p \cdot \boldsymbol{v}_p + \boldsymbol{T}_p \cdot \boldsymbol{\omega}_p \right). \tag{12}$$

The determination of $\boldsymbol{F}_p$ and $\boldsymbol{T}_p$ as well as the coupling between the particles and the fluid are inherently different in DPFS and PPMs. The details will be described in Sec. 3.2.

3 Numerical Modeling

First, the fundamentals of the flow solver are discussed and then, a modification of the discretization is proposed, by which the numerical dissipation error can be controlled to obtain an accurate implicit sgs model for LES. Subsequently, the numerical approximation of the particle dynamics used by DPFS and the PPM will be compared. For details on the numerical schemes of the DPFS, the reader is referred to [43]. The solution scheme for Eq. 1 is based on a cell-centered finite-volume discretization on hierarchical Cartesian grids which has been described and validated in a series of papers [24, 44, 43]. The conservative variables $\boldsymbol{Q}$ in Eq. 1 are integrated in time using an explicit five-step predictor-corrector Runge-Kutta method [43]. The fluxes are divided into an inviscid part $\bar{\boldsymbol{H}}_{\mathrm{inv}}$ and a viscous part $\bar{\boldsymbol{H}}_{\mathrm{visc}}$ as described by Eq. 2. The inviscid fluxes are again divided into the convective and the pressure terms and computed by a variant of the AUSM [32] of second-order accuracy as proposed by [36]. For the inviscid fluxes, the primitive variables at the cell surfaces are extrapolated according to the MUSCL scheme [31], while the extrapolation uses the cell-centered gradients of the primitive variables obtained by a second-order least-squares approach [43]. The viscous fluxes are discretized with central differences using mixed three-point and five-point stencils to obtain approximations of the gradients at the cell-surfaces.

3.1 Implicit large-eddy simulation

Spatial filtering of Eq. 1 leads to the concept of LES, where the impact of unresolved small scales on the resolved large scales has to be modeled via a suitable sgs

model. In this study, the MILES approach is employed, where the sgs model is implicitly incorporated in the numerical discretization, i.e. the dissipative truncation error of the numerical scheme serves as a sgs model. A careful validation of the MILES approach using the schemes described in the previous section has been performed and has been successfully applied in e.g. [41,42,37]. However, preliminary simulations have shown, that isotropic decaying turbulence is not accurately resolved due to the numerical dissipation added by the AUSM. It is well-known, that shock capturing methods are highly dissipative at low Mach numbers (e.g. [55]), and more precisely that the kinetic energy dissipation rate of these methods scales with the speed of sound [52]. As a remedy, a simple modification of the reconstruction of the extrapolated velocities $u_{L/R}$ at the left and right cell surfaces has been proposed in [54]. After extrapolating the cell-centered velocities onto the cell surfaces, the extrapolated velocities $u_{L/R}$ are redefined by

$$u_L^* = \frac{u_L + u_R}{2} + z \frac{u_L - u_R}{2},$$
$$u_R^* = \frac{u_L + u_R}{2} + z \frac{u_R - u_L}{2}, \tag{13}$$

where $u_{L/R}^*$ are the altered surface velocities, which are subsequently used in the discretization of the convective fluxes, and z can be a function satisfying $z \leq 1$. Unlike in [54], z will be chosen

$$z = min(\ 1,\ \lambda\ max(\ M_r^n, M_l^n\ )\ ), \tag{14}$$

with the normal Mach numbers $M_{r,l}^n$ at the cell surfaces and λ as a grid resolution dependent constant. A value of $z = 1$ recovers the original MUSCL scheme whereas for z tending to zero the surface velocities are obtained by a central difference such that velocity jumps are smoothed out. In contrast to [54], an additional parameter λ is added to control the dissipation for different grid resolutions. As in [54], the Mach numbers $M_{r,l}^n$ eliminate the speed of sound in the truncation error, and thus the amount of artificial numerical dissipation, whereas λ serves as a sgs model parameter to control the grid resolution dependent dissipation. With growing λ, the scheme behaves increasingly dissipative, or a decreasing λ centralizes the discretization of the convective fluxes substantially.

In Sec. 4.1, it will be shown that isotropic decaying turbulence can be accurately computed by the MILES approach, if λ is appropriately chosen. Finally, note that the modified AUSM proposed in [36] offers a similar parameter for the pressure flux. Numerical tests, however, indicate that the numerical dissipation added by the discretization of the pressure fluxes is negligible in decaying isotropic turbulence (not shown here).

3.2 Particle dynamics

In this section, the discretization of the equations describing the particle dynamics shown in 2.2 are introduced. First, a brief description for DPFS is provided. Subsequently, the Lagrangian two-way coupled PPM is described. The main assumptions of two-way coupled PPMs are discussed and shortcomings are analyzed.

(a)   (b)
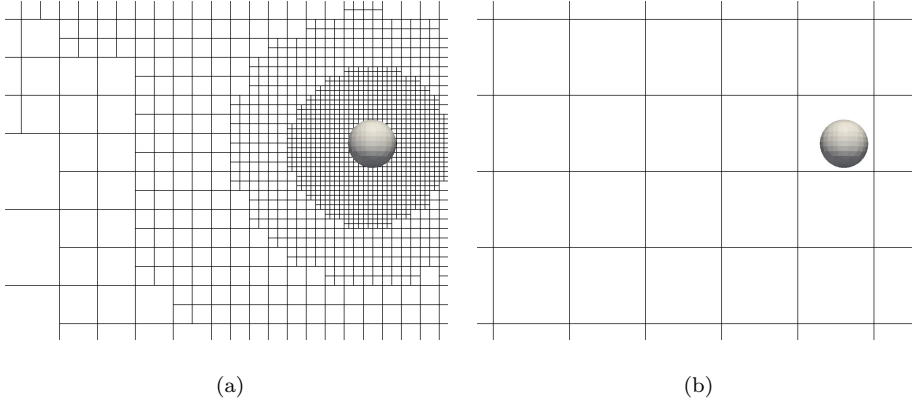
Fig. 1 Comparison of the DPFS approach and the PPM: (a) a dynamically refined Cartesian mesh is employed in the DPFS approach and the particle surfaces are represented by reshaped Cartesian cells. The no-slip condition is established at the particle surfaces and cells within the solid frame are discarded during the simulation. Compared to a DNS of the single phase isotropic decaying turbulence, four additional refinement levels are required to achieve an accurate representation of particles of Kolmogorov-length-scale size; (b) in simulations using the PPM, a static mesh is employed, which only resolves the background flow field. The illustration shows a DNS mesh with the grid cell length Δ_{DNS} and the ratio of the particle diameter to the cell length is $d_p/\Delta_{DNS} = 0.63$. The particles are not resolved and the impact of the particles on the flow field is modeled by a feedback force, which is exerted on the neighboring cells

3.2.1 Fully resolved particle dynamics

Figure 1a illustrates the DPFS approach. The mesh is dynamically refined in the vicinity of the particles. The interfaces of the particles are resolved by Cartesian cut-cells, which are reshaped to describe the particle surface, and all cells within the solid frame are discarded in the simulation. Due to the sharply resolved particle surface, mass and momentum are fully conserved in the DPFS method. The no-slip condition is established such that the force $\boldsymbol{F}_p$ and the torque $\boldsymbol{T}_p$ given in Eqs. 10 and 11 can be directly obtained by summation over all discrete particle surface segments $A_i, i \in \Gamma_p$, with

$$\boldsymbol{F}_p = \sum_{i \in \Gamma_p} \left[-p\boldsymbol{n} + \bar{\boldsymbol{\tau}} \cdot \boldsymbol{n} \right]_i A_i, \tag{15}$$

$$\boldsymbol{T}_p = \sum_{i \in \Gamma_p} \left[(\boldsymbol{x} - \boldsymbol{x}_p) \times (-p\boldsymbol{n} + \bar{\boldsymbol{\tau}} \cdot \boldsymbol{n}) \right]_i A_i. \tag{16}$$

Following [43], Eqs. 7 and 8 are solved by the predictor-corrector scheme of second-order accuracy and coupled with Eq. 1. The collision model proposed in [22] is employed to avoid overlapping bodies.

3.2.2 Point-particle models

The no-slip condition is not available in the PPM, i.e., it has to be modeled. A popular simplification of the semi-empirical Maxey-Riley equation [35] will be used

$$\boldsymbol{F}_{\mathrm{pp}} = 3\pi\mu d_{\mathrm{p}}(\boldsymbol{u}_p - \boldsymbol{v}_p)\phi(Re_{\mathrm{p}}), \tag{17}$$

which represents the quasi-steady Stokes drag augmented by the Schiller-Naumann drag correlation $\phi(Re_{\mathrm{p}}) = 24/Re_p(1 + 0.15Re^{0.687})$ for finite particle Reynolds numbers Re_{p} [10] and the undisturbed fluid velocity at the particle position $\boldsymbol{u}_p$. The accuracy of Eq. 17 as well as the full Maxey-Riley equation have been extensively analyzed for two-way and one-way coupled PPM in turbulent flows. It has been shown in [2,15] that the Stokes drag considered in Eq. 17 is the dominating contribution in the Maxey-Riley equation for high density ratios. The validity of Eq. 17 is, however, restricted to particles which are smaller than the smallest scale of the flow field η_k. As described in the Introduction, several studies indicate that Eq. 17 is capable to predict the mean value of the overall forces acting on the particle, while the rms-values of the force may be significantly different. The implications of these inaccuracies on two-way coupling have not been studied, yet. In general, the torque $\boldsymbol{T}_p$ acting on the point particles could be included into the dynamics of point particles [1]. However, no correlations for finite fluid inertia are known and with $\boldsymbol{T}_p \sim d_p^3$ in Stokes flow, spherical particles with $d_p = \mathcal{O}(\eta_k)$ will have negligible impact on the carrier flow. Hence, the rotational dynamics will be neglected in simulations using PPM. In this study, the subgrid kinetic energy of the LES is small and thus, the filtered velocity field may be used in Eq. 17 as pointed out in [57,3,16].

Figure 1b illustrates the PPM. In contrast to DPFS, the feedback of the particles on the flow field has to be modeled. Therefore, the force F_{pp} acting on the point particles is inserted into Eq. 1 in an action-reaction sense, i.e., the force is projected onto the underlying grid. Neglecting the rotational dynamics of the particles, the resulting transport of kinetic energy into the flow field due to the presence of a point particles yields

$$\psi_{pp} = \boldsymbol{F}_{pp} \cdot \boldsymbol{u}_p. \tag{18}$$

Several shortcomings may be identified for this approach. First, by projection of the force, the undisturbed fluid velocity $\boldsymbol{u}_p$ becomes an unknown, i.e., the flow field is locally changed by self-induced disturbances of the particles. To mitigate self-induced disturbances, a smooth force distribution like in [34] is applied. After determination of F_{pp} for each particle using Eq. 17, a distance-weighted feedback force F_{proj} is exerted on the neighboring cells i, with

$$\boldsymbol{F}_{\mathrm{proj,i}} = \boldsymbol{F}_{\mathrm{pp}} \cdot \frac{e^{-\left(d_{\mathrm{i}}^2/(\sigma\Delta^2)\right)}}{\sum_i e^{-\left(d_{\mathrm{i}}^2/(\sigma\Delta^2)\right)}}, \tag{19}$$

where d_{i} denotes the distance of the particle to the center of the cell i, Δ is the cell width, and σ is a smoothing parameter. Preliminary studies have shown that a small σ produces systematic errors due to self-induced disturbances and F_{pp} is generally underestimated. However, all statistics presented in Sec. 4 have been nearly identical for $\sigma = 4$ and $\sigma = 8$, which demonstrates that self-induced disturbances are mostly avoided.

Second, in LES only the filtered velocity field is resolved. Even if the subgrid turbulent kinetic energy of the LES is small and the particle dynamics are accurately recovered in LES, the projection method defined by Eq. 19 is applied to a larger physical region, since the cell size Δ is different for LES, i.e., the projection method is not independent of the grid size. A validation of the two-way coupling PPM in LES for small subgrid turbulent kinetic energy will be shown in Sec. 4.4.

Third, the projection of the force is not uniquely defined and depends on the particular implementation. Especially for finite-size particles, which are capable to distort eddies, it is not clear whether a force projection is suited to capture the turbulence modulation mechanisms due to the no-slip and impermeability conditions including displacement and viscous effects. Therefore, the validity of a force projection will be discussed in Secs. 4.2 and 4.3.

4 Results and discussion

In this section, the validation of the Lagrangian two-way coupled PPM will be discussed. After presenting the flow configuration, the MILES method introduced in Sec. 3.1 will be validated for single-phase simulations. Subsequently, the results of the DPFS in [45] will be compared with DNS using PPM findings. Therefore, a consistency analysis of the turbulent kinetic energy budgets is presented in physical and in spectral space. Finally, the PPM will be applied for LES and compared with the DPFS. In the following, the DNS using PPM is referred to PP-DNS, and the LES using PPM is denoted PP-LES.

The flow field of a threefold periodic cube with an edge length of L is initialized randomly and divergence free while fulfilling the realizability conditions [47]. The initialization procedure follows the method proposed by [39], where a prescribed energy spectrum $E(\kappa)$ serves as initial condition with the model spectrum

$$E(\kappa) = \left(\frac{3u_0^2}{2}\right)\left(\frac{\kappa}{\kappa_{\mathrm{p}}}^2\right)\exp\left(-\frac{\kappa}{\kappa_{\mathrm{p}}}\right), \qquad (20)$$

with the wave number $\kappa = |\boldsymbol{\kappa}|$ including the wave number vector $\boldsymbol{\kappa}$, the peak wave number κ_{p}, and the initial dimensionless rms-velocity u_0. The peak wave number is chosen $\kappa_{\mathrm{p}} = 4\kappa_0$ with $\kappa_0 = 2\pi L$, whereas u_0 is set to $u_0 = 0.1a$ with the speed of sound a. The pressure field is computed by solving the Poisson equation in spectral space [47] and the density field is obtained assuming an isothermal flow field. The initial microscale Reynolds number is set to $Re_{\lambda 0} = u_0\rho_{\mathrm{f}}\lambda_0/\mu = 79$. Note that the initial Taylor microscale λ_0 is uniquely defined by the generated initial velocity field. Thus, the viscosity μ has to be computed from the the initial microscale Reynolds number. The model spectrum Eq. 20 has been the basis for several comparable studies [17,33,50]. An excellent agreement of the DNS single phase results with these studies has been demonstrated in [43]. For the DNS, the same initial flow field has been used as in [45], while for LES the initial spectrum is spectrally cut off at the highest resolvable wave number. Four resolutions are used for the validation of PPM, where a 256^3 cells mesh corresponds to a DNS. Meshes using 128^3, 96^3, and 64^3 cells correspond to the LES cases LES$_{128}$, LES$_{96}$, and LES$_{64}$. For the LES, the same time step has been used as in DNS to achieve a higher transferability of the statistics, whereby the solution has a negligible

dependence on the reduced CFL number. The accuracy of the MILES model for the three LES cases will be presented next.

4.1 Monotone implicit LES

The prerequisite for PP-LES is an accurate subgrid model. Therefore, the implicit model, which has been presented in Sec. 3.1, will be validated in this section. The parameter λ for the convective terms proposed in Sec. 3.1 is defined based on the objective to resolve major characteristics of decaying isotropic turbulence accurately by the LES. The coarsest resolution of the LES is chosen such that the energy containing wave numbers are well resolved. This ensures that the turbulent kinetic energy $E_{\mathrm{k}} = \int_0^\infty E(k)\mathrm{d}k = \langle \boldsymbol{u'}^2/2 \rangle$, where the brackets $\langle \ \rangle$ denote the spatial ensemble average and $\boldsymbol{u'}$ the rms-velocity vector, is nearly constant for all resolutions, i.e., the subgrid kinetic energy is negligible. After the initialization, the turbulent kinetic energy decays, since no production term is present and the turbulent kinetic energy budget reads

$$\frac{\partial E_k}{\partial t} = -\mathcal{E}. \tag{21}$$

The integral viscous dissipation rate of incompressible flows can be determined by integrating the local dissipation rate ϵ over the fluid domain V_f, i.e.,

$$\mathcal{E} = \int_{V_f} \epsilon dV = \int_{V_f} 2\mu \bar{\boldsymbol{S}} : \bar{\boldsymbol{S}} dV, \tag{22}$$

where $\bar{\boldsymbol{S}} : \bar{\boldsymbol{S}}$ denotes the inner product of the strain-rate tensor defined in Sec. 1.

Figures 2a and 2b demonstrate the single phase performance of the LES compared to the DNS results, which have been validated in [43]. Figure 2a shows the the turbulent kinetic energy E_k normalized by its initial value $E_{k,0}$ over the nondimensional time $t^* = t\epsilon_0/u_0^2$ using the initial viscous dissipation rate ϵ_0. An excellent agreement with the reference solution from DNS can be observed. Consequently, the temporal development of the decay rate of the turbulent kinetic energy (Fig. 2b) matches well with the DNS. The decay rate is normalized by the reference viscous dissipation rate $\epsilon_{ref} = \rho u_0^3/L$. Figure 2c illustrates the skewness $-S_3$ of the velocity derivative

$$S_3 = \frac{\langle (\partial u_i/\partial x_i)^3 \rangle}{\langle (\partial u_i/\partial x_i)^2 \rangle^{3/2}}. \tag{23}$$

The LES of the three resolutions are compared with the DNS data. After a few time steps, the skewness converges to a constant grid dependent level. The skewness of the velocity derivative is directly connected to effects concerning the energy cascade including vortex stretching and the transfer of energy between different scale [40]. The theoretically determined negative constant value is confirmed by experiments for the Reynolds number analyzed in this study [56]. For LES of decaying isotropic turbulence, it is observed for different turbulence models that the skewness diminishes with decreasing resolution (e.g. [21], [53]). This behavior
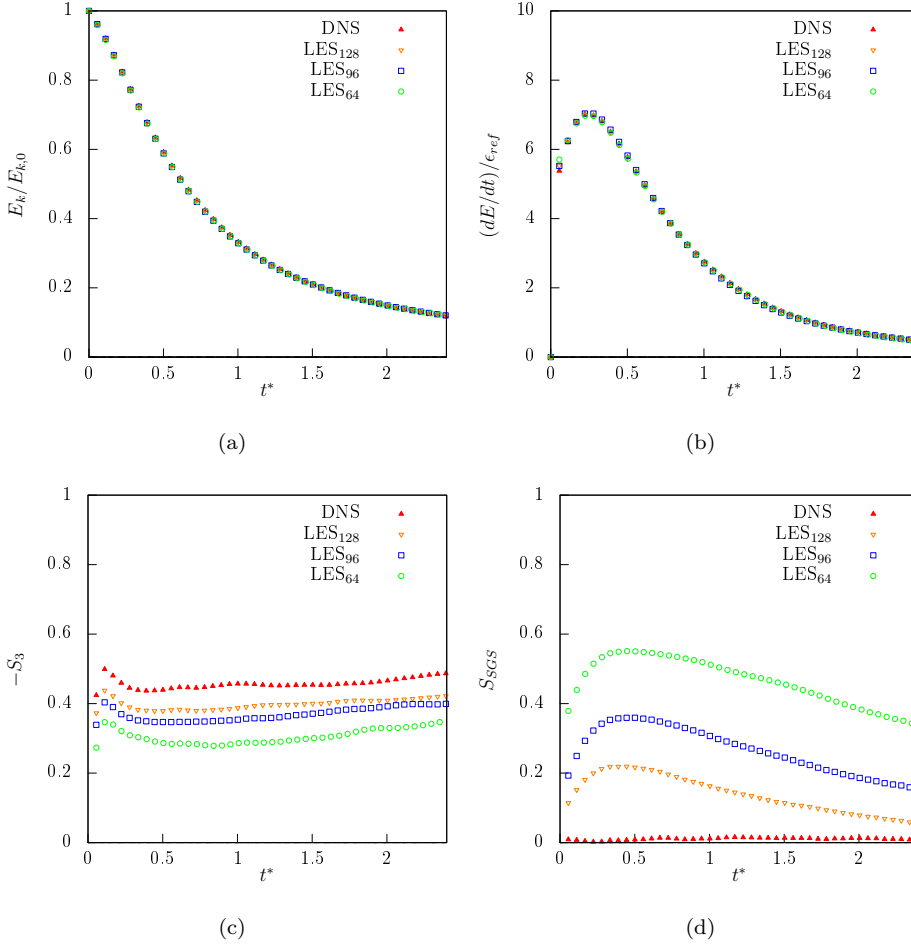
Fig. 2 Comparison of the LES with DNS for single phase isotropic decaying turbulence. Nondimensional temporal development of: (a) turbulent kinetic energy $E_k(t)$ normalized by its initial value $E_{k,0}$; (b) turbulent kinetic energy decay rate dE/dt normalized by the reference viscosity $\epsilon_{ref} = \rho u_0^3/L$; (c) velocity derivative $-S_3$; and (d) subgrid activity S_{sgs}

is also indicated in Fig. 2c.

The subgrid activity S_{sgs} from [20]

$$S_{\text{sgs}} = \frac{\mathrm{d}E_{\text{k}}/\mathrm{d}t - \mathcal{E}_\mu}{\mathrm{d}E_{\text{k}}/\mathrm{d}t}, \tag{24}$$

will be adopted to quantify how much the turbulence model affects the behavior of the LES. The quantity $\mathcal{E}_\mu = 2\nu \int_{V_f} 2\mu \widehat{\widehat{\boldsymbol{S}}} : \widehat{\widehat{\boldsymbol{S}}} dV$ denotes the resolved part of the viscous dissipation rate $\mathcal{E}$. The value $S_{\text{sgs}} = 0$ identifies a DNS, whereas $S_{\text{sgs}} = 1$ refers to an LES at infinite Reynolds number, i.e., due to scale separation all viscous effects occur at infinitely high wave numbers and thus, have to be modeled. Figure 2d shows the subgrid activity S_{sgs} for the LES compared to a DNS. The
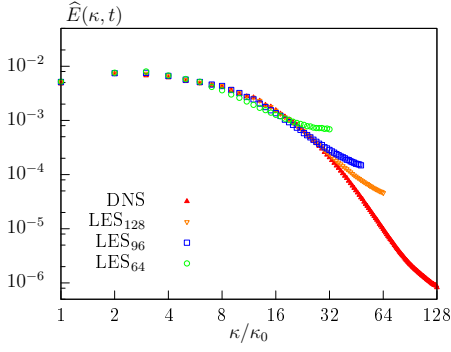
Fig. 3 Three-dimensional energy spectrum $\widehat{E}(\kappa, t)$ at $t^* = 1.0$

subgrid activity of the DNS vanishes, whereas a decreasing resolution results in an increasing subgrid activity. Note that $S_{\mathrm{sgs}} = 1$ is unlikely to be realized for $Re_\lambda = \mathcal{O}(50)$, since energy containing scales and dissipative scales partially overlap [6].

Suspended particles are known to interact with a range of wave numbers, which is why the turbulent kinetic energy spectrum of the LES is important. Figure 3 shows the turbulent kinetic energy spectra of the LES compared with the results of the DNS. The LES$_{128}$ exhibits accurate results for a broad range of wave numbers. Only at the highest wave numbers, the turbulent kinetic energy accumulates and an overshoot is observed. The LES$_{64}$ solution shows good agreement at low wave numbers, moderate deviations at intermediate wave numbers, and also an overshoot at the highest resolved wave numbers. The numerical convective fluxes are progressively centralized and consequently, the numerical damping of high-frequency parts of the solution vanishes, which is indicated by the overshoot at the highest resolved wave numbers. Similar results are obtained for the explicit dynamic Smagorinsky model with a small filter width [12]. A higher λ could be chosen, which increases the subgrid kinetic energy. The impact of the modified energy spectrum will be discussed in Sec. 4.4.

It can be summarized that the MILES solutions of decaying isotropic turbulence show reliable results compared to a DNS. The major characteristics of the carrier flow are well predicted such that this setup can be used to analyze particle-laden flows.

4.2 Consistency analysis of turbulent kinetic energy budgets

The main purpose of this section is to analyze whether the projection of a force in two-way coupling models is appropriate to capture turbulence modulation by particles. Therefore, turbulent kinetic energy budgets of particle-laden flows are considered. For DPFS, the budget reads [45]

$$\frac{\partial E_k}{\partial t}(t) = \Psi(t) - \mathcal{E}(t), \tag{25}$$

where the total kinetic energy transfer $\Psi(t)$ on the particle surfaces can be computed by

$$\Psi(t) = \sum_{p=1}^{N_p} \psi_p = -\sum_{p=1}^{N_p} \left(\boldsymbol{F}_p \cdot \boldsymbol{v}_p + \boldsymbol{T}_p \cdot \boldsymbol{\omega}_p \right). \tag{26}$$

If the particles are accelerated by the fluid forces acting on the particle surface ψ_p acts as a local sink, otherwise it acts as a local source. The budget Eq. 25 can be only precisely evaluated, if all the particle and fluid scales are fully resolved. While $\Psi(t)$ is available in DPFS and could be computed in PP-DNS as well, $\mathcal{E}(t)$ includes the viscous dissipation rate of particle boundary layers and wakes and hence, is only available in DPFS. For PP-DNS, the turbulent kinetic energy budget has a different formulation [17], which is

$$\frac{\partial E_k}{\partial t}(t) = \Psi_{pp}(t) - \bar{\mathcal{E}}(t) = -\sum_{p=1}^{N_p} \boldsymbol{F}_{pp} \cdot \boldsymbol{U}_p - \bar{\mathcal{E}}, \tag{27}$$

with $\Psi_{pp}(t) = -\sum_{p=1}^{N_p} \psi_{pp}$. Unlike the budget in Eq. 25, only the background dissipation $\bar{\mathcal{E}}(t)$, which is the viscous dissipation rate excluding particle wakes and boundary layers, is part of Eq. 27. A comparison of the DPFS and PP-DNS solutions has to take into account the different budgets [58] and a direct comparison of $\bar{\mathcal{E}}(t)$ and $\mathcal{E}(t)$ reveals fundamental differences [46]. Therefore, the overall viscous dissipation rate $\mathcal{E}(t)$ is split into a particle induced dissipation $\mathcal{E}_p$, which is the dissipation in the vicinity of the particles due to the particle boundary layers and wakes, and the background dissipation, i.e.,

$$\mathcal{E}(t) = \bar{\mathcal{E}}(t) + \mathcal{E}_p(t). \tag{28}$$

The analysis of the particle induced dissipation $\mathcal{E}_p$ in [45] yields

$$\mathcal{E}_p(t) = \sum_{p=1}^{N_p} \boldsymbol{F}_p \cdot (\boldsymbol{U}_p - \boldsymbol{v}_p) + \boldsymbol{\mathcal{T}}_p \cdot (\boldsymbol{\Omega}_p - \boldsymbol{\omega}_p) + \mathcal{I}_f, \tag{29}$$

where $\mathcal{I}_f$ takes into account the fluid inertia terms and the remaining terms stem from hydrostatic and shear stress contributions. Equation 29 is valid for arbitrary particle geometries, which are not significantly larger than the smallest characteristic length scale. Using DPFS, it has been shown numerically, that Eq. 29 holds for the diameter considered here [45]. Neglecting the fluid inertia terms, a similar expression to Eq. 29 can be derived for Stokes flow conditions, which, however, is only valid for vanishing particle Reynolds numbers [27].
Inserting Eqs. 29 and 26 into the budget Eq. 25 yields

$$\frac{\partial E_k}{\partial t}(t) = \Psi_p(t) - \bar{\mathcal{E}}(t) - \mathcal{E}_p(t) = -\sum_{p=1}^{N_p} \boldsymbol{F}_p \cdot \boldsymbol{U}_p - \bar{\mathcal{E}}, \tag{30}$$

where the fluid inertia and the rotational particle dynamics have been neglected. Comparing Eq. 30 and Eq. 27 finally demonstrates that two-way coupled PPM provide a consistent modeling of particle-laden turbulent flow. The two-way coupling contribution $\Psi_{pp}(t)$ represents the combined effect of particle induced dissipation and the direct turbulent kinetic energy transfer, i.e., $\Psi_{pp}(t) \approx \mathcal{E}_p(t) + \Psi_p(t)$. This

analysis, however, uses several simplifications, which essentially limits its validity. For particle diameters $d_p > \eta$, higher particle Reynolds numbers Re_p, higher volume loadings ϕ_v, and non-spherical particles with higher aspect ratios, PPMs have to be validated carefully to provide additional information about its reliability. Additionally, no information about the scales involved in turbulence modulation and momentum exchange between particles and fluid has been gained.

In spectral space, the turbulent kinetic energy budget Eq. 27 reads for PPMs [17]

$$\frac{\partial \widehat{E}(\boldsymbol{\kappa}, t)}{\partial t} = \widehat{T}(\boldsymbol{\kappa}, t) + \widehat{\Psi}(\boldsymbol{\kappa}, t) - \widehat{\mathcal{E}}(\boldsymbol{\kappa}, t), \tag{31}$$

with $\widehat{E}(\boldsymbol{\kappa}) = \widehat{\boldsymbol{u}}(\boldsymbol{\kappa}) \cdot \widehat{\boldsymbol{u}}(\boldsymbol{\kappa})/2$, which can be obtained using the Fourier transformed velocity vector $\widehat{\boldsymbol{u}}(\boldsymbol{\kappa})$. The spectral energy transfer rate $\widehat{T}(\boldsymbol{\kappa}, t)$ represents the energy transfer between local and non-local wave numbers due to the convective terms [13] and $\widehat{\mathcal{E}}(\boldsymbol{\kappa}) = 2\mu\boldsymbol{\kappa}^2 \widehat{E}(\boldsymbol{\kappa})$ is the viscous dissipation rate in spectral space. The spectral fluid-particle interaction in PPM is defined by

$$\widehat{\Psi}(\boldsymbol{\kappa}) = -\mathrm{Re}\left\{\widehat{\boldsymbol{u}}(\boldsymbol{\kappa}) \cdot \widehat{\boldsymbol{f}}_{pp}(\boldsymbol{\kappa})\right\}, \tag{32}$$

where $\mathrm{Re}\left\{\cdot\right\}$ denotes the real part and $\widehat{\boldsymbol{f}}_{pp}(\boldsymbol{\kappa})$ is the Fourier transformed force vector acting on the particle. Summing all terms in Eq. 31 over spherical shells of radius κ and thickness $\Delta\kappa$ and taking only the real part into account yields the one-dimensional reduction of Eq. 31

$$\frac{\partial \widehat{E}(\kappa, t)}{\partial t} = \widehat{T}(\kappa, t) + \widehat{\Psi}(\kappa, t) - \widehat{\mathcal{E}}(\kappa, t). \tag{33}$$

Equation 33 can be directly computed in PP-DNS by Fourier transformation. To evaluate Eq. 33 in DPFS, however, the velocity field has to be first filtered to a uniform mesh, i.e. at the resolution of the PP-DNS. Unlike in [45], a Gaussian filter is applied, where the filter width is chosen, such that a filtering operation of single phase DNS does not alter the energy spectrum. Similar to the turbulent kinetic energy budget in real space, $\widehat{\Psi}(\kappa, t)$ represents the combined effect of particle induced dissipation and direct transfer of kinetic energy. Therefore Eq. 33 can not be directly analyzed in particle resolved simulations consistent to the PPM. Due to the resolved boundary layers, the velocity field comprises high frequency components, as observed in [33], and the direct evaluation of $\widehat{\Psi}(\kappa, t)$ yields a high frequency positive contribution as in [45]. Moreover, it is not clear, how a Fourier transformed velocity field can be obtained in the presence of fully-resolved particles, where no fluid field exists in the solid phase. A consistent formulation of Eq. 33 for particle resolved simulations is, however, obtained, if the velocity field in the vicinity of the particles is locally overwritten with the velocity seen by the particles $\boldsymbol{U}_p$. For this study, the velocity $\boldsymbol{u}(\boldsymbol{x})$ in the vicinity of a particle is modified according to

$$\boldsymbol{u}(\boldsymbol{x}) = \begin{cases} \boldsymbol{U}_p & r \leq r_t \\ w(r) \cdot \boldsymbol{U}_p + (1 - w(r)) \cdot \boldsymbol{u}(\boldsymbol{x}) & r_t < r < R_t \\ \boldsymbol{u}(\boldsymbol{x}) & R_t \leq r \end{cases}, \tag{34}$$

where $w(r)$ is a smooth weighting function containing the distance $r = |\boldsymbol{x} - \boldsymbol{x}_p|$ and r_t and R_t are lower and upper radial bounds. Note that this modification

Table 1 Parameters of the particle-laden simulations performed in [45] at injection time $t_i^* = 0.28$: number of particles N_p, density ratio particle-to-fluid ρ_p/ρ, ratio of the particle diameter d_p to the Kolmogorov length scale η, the integral length scale ℓ, the grid cell length of the DNS Δ_{DNS}, the volume fraction ϕ_v, and the mass fraction ϕ_m of the particles

Case	N_p	ρ_p/ρ	d_p/η	d_p/ℓ	d_p/Δ_{DNS}	ϕ_v	ϕ_m
1	45,000	40	1.32	0.032	0.63	$3.5 \cdot 10^{-4}$	0.014
2	45,000	200	1.32	0.032	0.63	$3.5 \cdot 10^{-4}$	0.07
3	45,000	1000	1.32	0.032	0.63	$3.5 \cdot 10^{-4}$	0.35
4	45,000	5000	1.32	0.032	0.63	$3.5 \cdot 10^{-4}$	1.75

merely alters the velocity field in the post-processing stage, i.e., during the DPFS Eq. 34 is not applied. Equation 34 introduces additional filtering effects, which, however, are negligible for small particles and dilute suspensions. Note that the spectra obtained by Eq. 34 are quite insensitive to the exact definition of $w(r), r_t$, and R_t.

4.3 Validation of DNS using point-particle models

In this section, the PP-DNS solutions are compared with the results of the DPFS in [45]. Beside the assessment of the accuracy of PP-DNS, the purpose of the section is to identify the turbulent scales, which are affected by the presence of the particles. This has important implications for the PP-LES, which is presented thereafter.

Four particle-laden cases are considered. Table 1 lists the non-dimensional parameters related to the particles. The simulations in [45] will be referred to as "DPFS Case", whereas the PP-DNS will be referred to "PP-DNS Case". The single phase DNS is denoted "sP-DNS". 45,000 particles are injected at $t^* = 0.28$ into the isotropic turbulent flow field. Following [45], the particle velocities are initialized with the local fluid velocity. The particle-to-fluid density ratio ρ_p/ρ is varied in the four cases, whereas the particle diameter d_p, and hence the volume fraction of the particles ϕ_v are held constant with $\phi_v = 3.5 \cdot 10^{-4}$. The setup is assigned to the two-way coupling regime [14].

Figure 4 shows the turbulent kinetic energy E_k normalized by its initial value $E_{k,0}$. Clearly, the modulation of the turbulent kinetic energy by particles is correctly predicted by PP-DNS for all cases and the deviations between the PP-DNS and the DPFS are negligible. For this parameter range, the main mechanisms of turbulence modulation are the direct transfer of kinetic energy between the solid and the fluid frame as well as the increased dissipation due to the boundary layers of the particles.

Figure 5 displays the total kinetic energy of the particles $K(t)$ normalized by $K_0 = \phi_m E_{k,0}$. Like E_k, the kinetic energy of the particles is well captured by the PP-DNS. Even for the cases 1 and 2, where the requirement $\rho_p \gg \rho$ for Eq. 17 might be not strictly fulfilled, the kinetic energy of the particles is accurately predicted. For cases 3 and 4, a systematic overestimate of a few percent are observed. The particle Reynolds number for all cases is $Re_p = \mathcal{O}(5)$ and the turbulence modulation mechanisms for this parameter range is determined by the increased
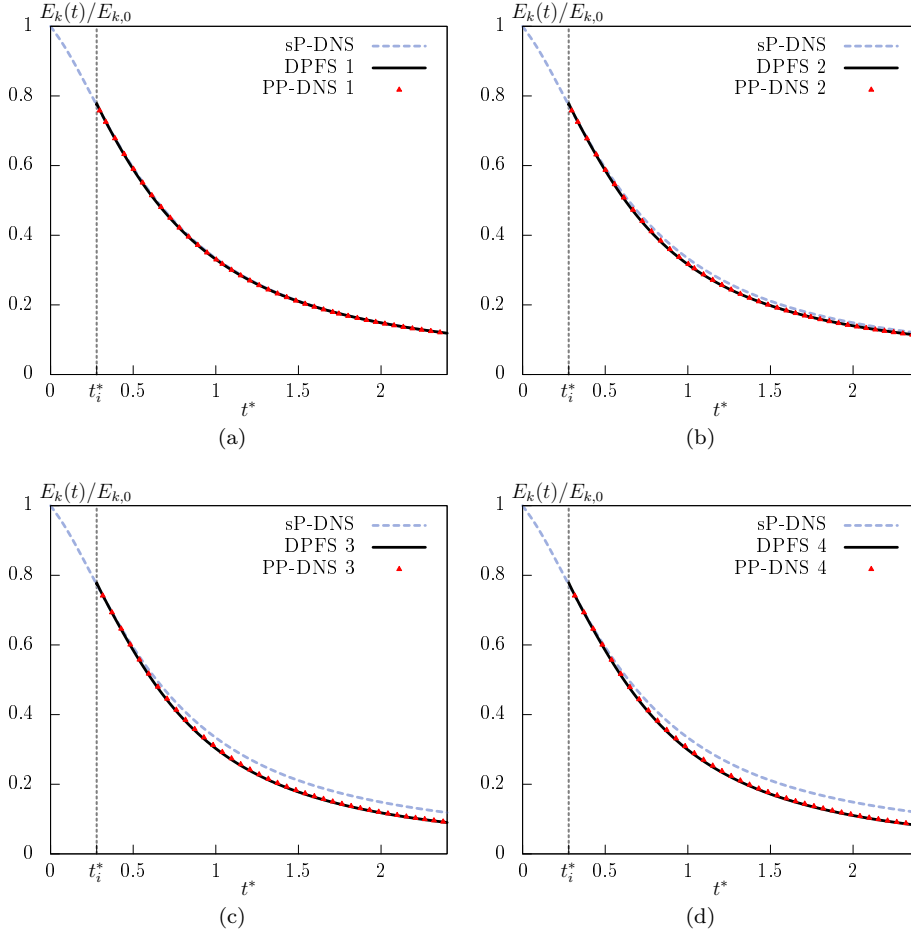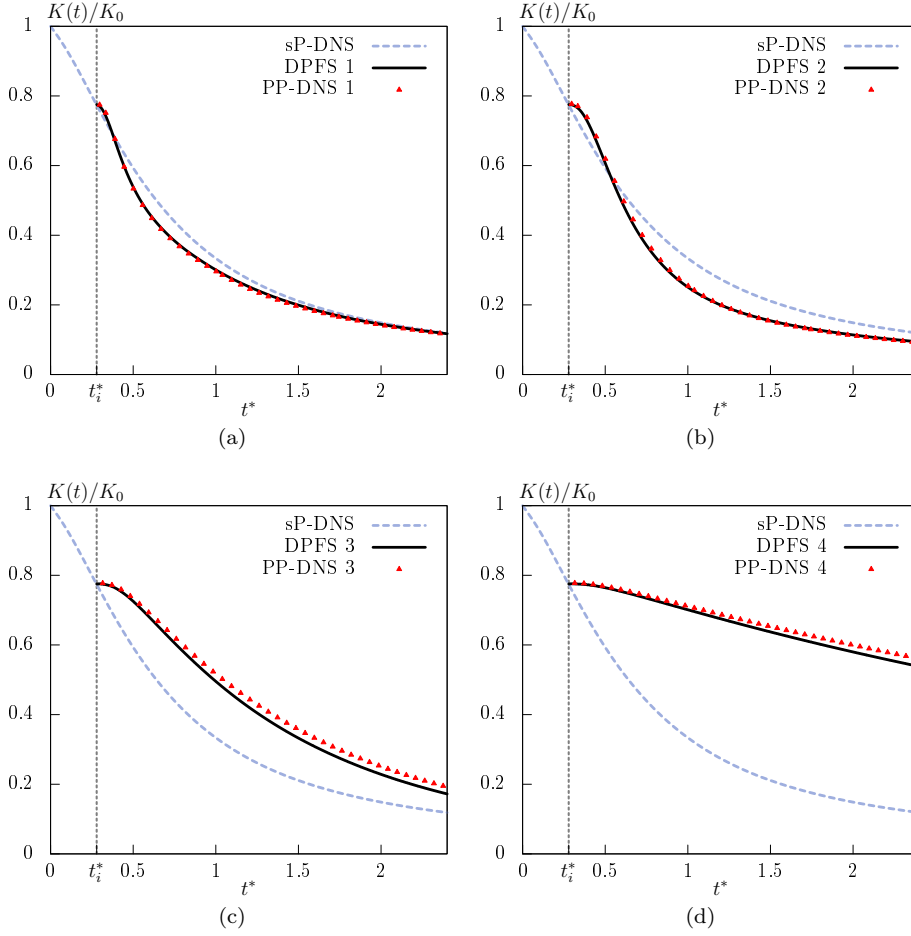
Fig. 4 Temporal development of the turbulent kinetic energy $E_k(t)$ normalized by its initial value (cases 1 - 4 in (a) - (d) respectively)

dissipation due to the particle drag and the direct transfer of kinetic energy. Both are consistently captured by the PPM as shown in the previous section, which explains the good accuracy of the PP-DNS.

In Fig. 6, the three-dimensional energy spectra for case 3 are compared. Good agreement can be observed between the results of PP-DNS and the DPFS. As a reference, the energy spectrum of the single phase DNS at a time step with the same levels of turbulent kinetic energy as in the DPFS and the PP-DNS is shown. While the PP-DNS and the single phase spectra almost perfectly overlap, the highest wave number components of the DPFS are damped. This damping stems from the filtering process and the application of Eq. 34. The energy spectra of the unfiltered DPFS data show enhanced high wave number components [45]. The almost perfect agreement of the PP-DNS with the single phase spectrum proves, that the smoothing of the force projection Eq. 19 successfully mitigates any high

Fig. 5 Temporal development of the total kinetic energy of the particles $K(t)$ normalized by $K_0 = \phi_m E_{k,0}$ (cases 1 - 4 in (a) - (d) respectively)

frequent disturbances.

Figure 7 shows the spectral fluid-particle interaction rate $\widehat{\Psi}(\kappa, t)$. For all cases, the PP-DNS is in good agreement with the DPFS. The PP-DNS correctly predicts the energy reduction at wave numbers $\kappa < 32$. Only at higher wave numbers, the DPFS shows some positive contributions, which, however, are considerably smaller than in [45] due to the modification by Eq. 34. The main contribution of the fluid-particle interaction occurs at larger scales. Although the interactions at the particle scale reveal complex features including regions of high strain rates and regions containing locally attenuated as well as augmented turbulent kinetic energy [45], the energy spectrum is mainly altered at low wave numbers. This finally explains the excellent agreement of the PP-DNS and the DPFS. At the length scale of low wave numbers, the particular turbulence modulation at the Kolmogorov-scale is insignificant as long as the combined effect of particle induced viscous

$\widehat{E}(\kappa, t)$

sP-DNS
DPFS 3
PP-DNS 3

κ/κ_0
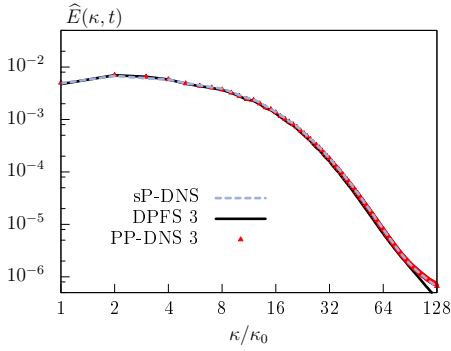
Fig. 6 Three-dimensional energy spectrum $\widehat{E}(\kappa, t)$ at $t^* = 1.0$ for $\rho_p/\rho = 1000$. The single phase spectrum is taken at a time step with the same turbulent kinetic energy level as the DPFS and the PP-DNS


$\widehat{\Psi}(\kappa) = Re\left\{\widehat{\boldsymbol{u}} \cdot \widehat{\boldsymbol{f}}(\boldsymbol{\kappa})\right\}$

DPFS 3
PP-DNS 3

κ/κ_0
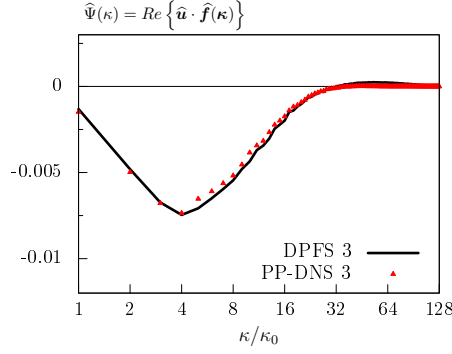
Fig. 7 Three-dimensional fluid-particle interaction spectrum $\widehat{\Psi}(\kappa, t)$ at $t^* = 1.0$

dissipation $\mathcal{E}_p$ and the direct transfer of kinetic energy Ψ is correctly predicted. The strong match of the energy spectra of the single phase and the PP-DNS shows that the energy cascade of the single phase dominates. Furthermore, the fluid particle-interaction spectrum shows negligible deflections for $\kappa > 32$. Therefore, the PP-LES should be capable to predict the DPFS results. This will be discussed next.

4.4 Validation of LES using point-particle models

In this section, the results of the PP-LES will be compared with the DPFS and the PP-DNS data. After identifying the turbulent scales affected by particles, the main questions stated in the introduction can be addressed. As already indicated in the previous section, the single phase turbulent cascade dominates in the particle-laden cases. Furthermore, PPMs mainly affect the small wave numbers and sgs models act on the highest wave numbers. Consequently, the PPMs and sgs models should not directly affect each other. Additionally, this section will provide information, whether the accuracy of the PP-LES is affected by the resolution. For conciseness, only case 3 will be shown, since the general trend for the other cases is similar to that of case 3.

Figure 8 shows the temporal development of the turbulent kinetic energy E_k. The PP-LES correctly predicts the turbulence modulation for all resolutions. A comparison of the mean total kinetic energy of the particles is shown in Fig. 9. Every PP-LES resolution is in good agreement with the PP-DNS, and a few percent deviation between the simulations using PPM and the DPFS are observed. The probability density function (pdf) of the velocity magnitude of the particles $|\boldsymbol{v}_p|$ at $t^* = 1.0$ is shown in Fig. 10. Again, the LES resolution has only a minor impact on the performance of the PPM. The mean absolute value is overestimated by 0.66% in the PP-DNS, and by 1.65% in the PP-LES$_{64}$, and the rms value by 0.63% in the PP-DNS, and by 1.64% in the PP-LES$_{64}$. This is within the uncertainty due to the limited number of particles. Figure 11 shows the alignment of
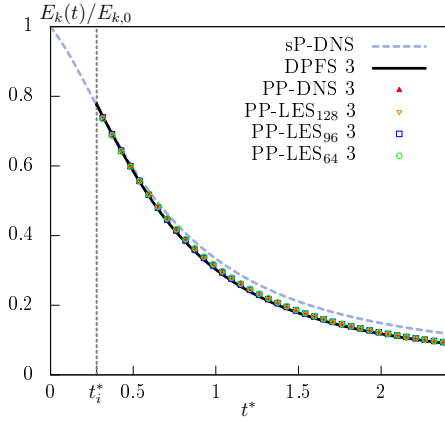
Fig. 8 Comparison of the turbulent kinetic energy $E_k(t)$ normalized by the initial turbulent kinetic energy $E_{k,0}$
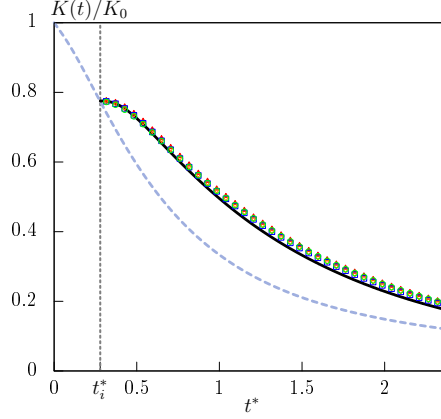
Fig. 9 Temporal development of the total kinetic energy of the particles $K(t)$ normalized by $K_0 = \phi_m E_{k,0}$. For an interpretation of the line types, see Fig. 8
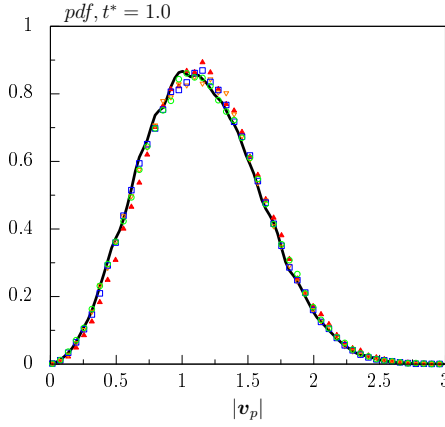
Fig. 10 Probability density function (pdf) of the absolute value of the particle velocity $\boldsymbol{v}_p$ at $t^* = 1.0$. For an interpretation of the line types, see Fig. 8
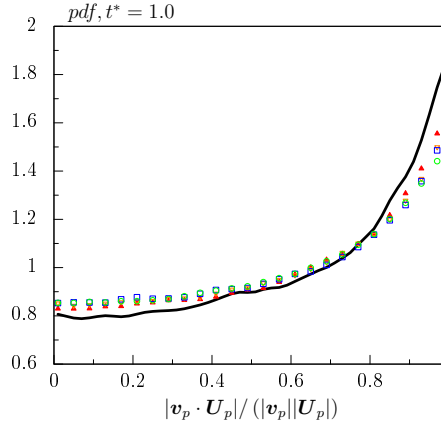
Fig. 11 Probability density function (pdf) of the alignment of the $\boldsymbol{v}_p$ with the velocity seen by particles $\boldsymbol{U}_p$. For an interpretation of the line types, see Fig. 8

the particle velocity $|\boldsymbol{v}_p|$ with the fluid velocity seen by the particles $|\boldsymbol{U}_p|$. Pronounced crossing-trajectory effects [11] can be observed and the majority of the particle trajectories are not aligned with the local fluid velocity. Compared to the PP-DNS, the PP-LES show good agreement. Note that a coarser mesh leads to a minor overestimate of the crossing trajectory effect. The DPFS predicts a stronger alignment of the particles with the fluid. A conclusive assessment is not possible though, since the measurement of $|\boldsymbol{U}_p|$ is intricate for fully resolved particles as discussed in Sec. 4.2.

Next, the accuracy of the DNS and LES data will be analyzed in spectral space. Figure 12 shows the energy spectra of the particle-laden cases. Like for the PP-DNS, the energy spectra are quite similar to the single phase spectra shown in
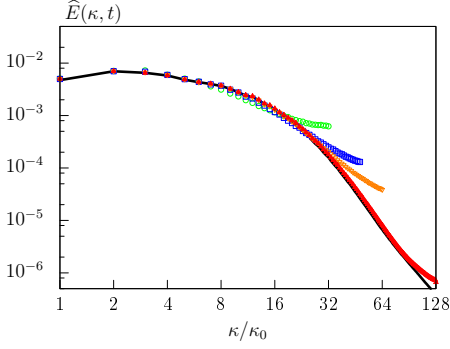
Fig. 12 Three-dimensional energy spectrum $\widehat{E}(\kappa, t)$ at $t^* = 1.0$ for $\rho_p/\rho = 1000$. For an interpretation of the line types, see Fig. 8
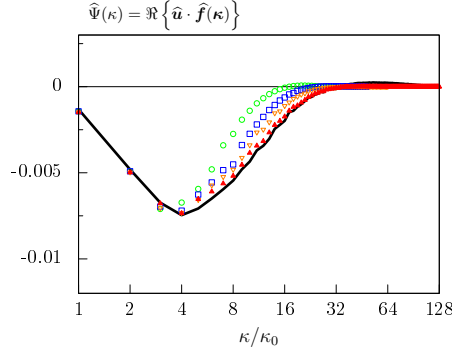
Fig. 13 Three-dimensional fluid-particle interaction spectrum $\widehat{\Psi}(\kappa, t)$ at $t^* = 1.0$ for case 3. For an interpretation of the line types, see Fig. 8
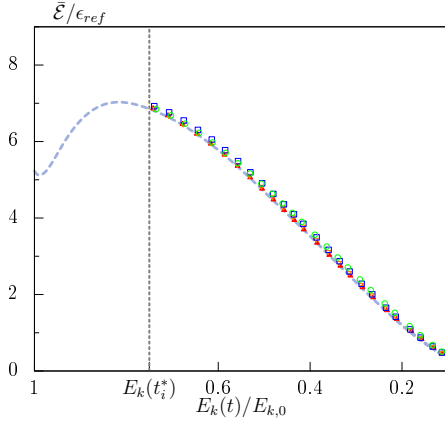
Fig. 14 Viscous background dissipation rate $\bar{\mathcal{E}}$ as a function of the turbulent kinetic energy E_k. For an interpretation of the line types, see Fig. 8

Fig. 3. Although the force projection is applied at the lowest resolved scales, no significant modulation of the energy spectra can be observed at the highest resolved scale. This is supported by the fluid-particle interaction spectrum $\widehat{\Psi}(\kappa, t)$ shown in Fig. 13. For the highest resolved wave numbers, the interaction spectrum vanishes even for the coarsest mesh, where the highest resolved wave numbers contain significant portions of turbulent kinetic energy. Moreover, the interaction spectrum shows considerable deviations for the different resolutions, although the trend is captured well.

The force projection in two-way coupling incorporates the feedback of the particles at the smallest scales. Potentially, this can disturb the sgs model of the LES. To assess the impact of the disturbances of the two-way coupling, the background viscous dissipation $\bar{\mathcal{E}}(t)$ is analyzed. According to Eq. 27, the background dissipation reads

$$\bar{\mathcal{E}}(t) = -\frac{\partial E_k}{\partial t}(t) + \Psi_{pp}(t), \qquad (35)$$

where the right-hand side is also determined in LES. For single phase isotropic decaying turbulence, the viscous dissipation rate is proportional to the turbulent

kinetic energy. This still holds for the particle-laden case, since the fluid-particle interaction spectrum mainly acts on the low wave numbers and the single phase turbulent cascade dominates as shown in Sec. 4.3. Figure 14 shows the background viscous dissipation rate $\bar{\mathcal{E}}$ over the turbulent kinetic energy for the simulations using PPM and for the sP-DNS. The particle-laden cases have approximately the same background viscous dissipation rate as the single phase simulation. That is, the PPM formulation does not induce additional significant disturbances in the setup analyzed here.

5 Concluding remarks

The accuracy of LES and DNS using a point-particle model including two-way coupling effects in isotropic decaying turbulence has been analyzed by comparison with the DPFS reference results using $45,000$ particles in [45]. The particle diameter is on the order of Kolmogorov scale. Thus, the point-particle approach is generally not justified. The current results, however, show that the simulations using point-particle models yield a promising accuracy even for larger particles.
A consistency analysis of the turbulent kinetic energy budgets has been performed, where budgets for fully-resolved particle-laden flows are compared with the two-way coupling approach. A force projection implicitly combines the particle induced dissipation and the direct transfer of kinetic energy on the surface of the particles, whereas fluid inertia terms are neglected. Therefore, a force projection is in general suited to recover the overall contribution of particle-fluid interaction for moderate particle Reynolds numbers.
The consistency analysis of the turbulent kinetic energy budgets has been extended towards the spectral space, which is valid for small particle diameters and dilute flows. A comparison of energy spectra of the DPFS, simulations using point-particle models, and single phase DNS showed that the single phase energy cascade dominates for the particle-laden cases. The largest portion of the fluid-particle interaction is located at low wave numbers. That is, the momentum exchange between particles and fluid at the smallest scales leads to turbulent modulation at large scales. Consequently, the complex interaction phenomena between particles and fluid at the smallest scales can be neglected as long as the net effect of the particle-fluid interaction is correctly predicted. In LES, the sgs model acts on the largest resolved wave numbers. Thus, the turbulence modulation predicted by two-way coupling does not interfere with the sgs model and the viscous dissipation of the background turbulent flow field is not altered by the force projection. The point-particle model proved to be robust for LES. Turbulence modulation as well as particle dynamics have been accurately reproduced by the point-particle model for all resolutions.
The present results are limited to one particle diameter, isotropic turbulence, spherical particles, and moderate particle Reynolds numbers. Further studies for a wide range of parameters and flow configurations are necessary to establish a profound evaluation of the accuracy of point-particle models. Consequently, additional benchmark cases similar as in [45] are required.

References

1. Andersson, H.I., Zhao, L., Barri, M.: Torque-coupling and particle–turbulence interactions. J. Fluid Mech. **696**, 319–329 (2012)
2. Armenio, V., Fiorotto, V.: The importance of the forces acting on particles in turbulent flows. Phys. Fluids **13**(8), 2437–2440 (2001)
3. Armenio, V., Piomelli, U., Fiorotto, V.: Effect of the subgrid scales on particle motion. Phys. Fluids **11**(10), 3030–3042 (1999)
4. Bagchi, P., Balachandar, S.: Effect of turbulence on the drag and lift of a particle. Phys. Fluids **15**(11), 3496–3513 (2003)
5. Bagchi, P., Balachandar, S.: Response of the wake of an isolated particle to an isotropic turbulent flow. J. Fluid Mech. **518**, 95–123 (2004)
6. Batchelor, G.: The Theory of Homogeneous Turbulence. Cambridge University Press (1953)
7. Boivin, M., Simonin, O., Squires, K.D.: Direct numerical simulation of turbulence modulation by particles in isotropic turbulence. J. Fluid Mech. **375**, 235–263 (1998)
8. Boivin, M., Simonin, O., Squires, K.D.: On the prediction of gas–solid flows with two-way coupling using large eddy simulation. Phys. Fluids **12**(8), 2080–2090 (2000)
9. Burton, T.M., Eaton, J.K.: Fully resolved simulations of particle-turbulence interaction. J. Fluid Mech. **545**, 67–111 (2005)
10. Clift, R., Grace, J.R., Weber, M.E.: Bubbles, drops, and particles. Courier Corporation (2005)
11. Csanady, G.T.: Turbulent diffusion of heavy particles in the atmosphere. J. Atmospheric Sci. **20**(3), 201–208 (1963)
12. Dairay, T., Lamballais, E., Laizet, S., Vassilicos, J.C.: Numerical dissipation vs. subgrid-scale modelling for large eddy simulation. J. Comput. Phys. **337**, 252–274 (2017)
13. Domaradzki, J.A., Rogallo, R.S.: Local energy transfer and nonlocal interactions in homogeneous, isotropic turbulence. Phys. Fluids A **2**(3), 413–426 (1990)
14. Elghobashi, S.: On predicting particle-laden turbulent flows. Appl. Sci. Res. **52**(4), 309–329 (1994)
15. Elghobashi, S., Truesdell, G.: On the two-way interaction between homogeneous turbulence and dispersed solid particles. i: Turbulence modification. Phys. Fluids A **5**(7), 1790–1801 (1993)
16. Fede, P., Simonin, O.: Numerical study of the subgrid fluid turbulence effects on the statistics of heavy colliding particles. Phys. Fluids **18**(4), 045,103 (2006)
17. Ferrante, A., Elghobashi, S.: On the physical mechanisms of two-way coupling in particle-laden isotropic turbulence. Phys. Fluids **15**(2), 315–329 (2003)
18. Garg, R., Narayanan, C., Lakehal, D., Subramaniam, S.: Accurate numerical estimation of interphase momentum transfer in lagrangian–eulerian simulations of dispersed two-phase flows. Int. J. Multiphase Flow **33**(12), 1337–1364 (2007)
19. Geurts, B., Kuerten, J.: Ideal stochastic forcing for the motion of particles in large-eddy simulation extracted from direct numerical simulation of turbulent channel flow. Phys. Fluids **24**(8), 081,702 (2012)
20. Geurts, B.J., Fröhlich, J.: A framework for predicting accuracy limitations in large-eddy simulation. Phys. Fluids **14**(6), L41–L44 (2002)
21. Geurts, B.J., Kuczaj, A.K., Titi, E.S.: Regularization modeling for large-eddy simulation of homogeneous isotropic decaying turbulence. J. Phys. A **41**(34), 344,008 (2008)
22. Glowinski, R., Pan, T., Hesla, T., Joseph, D., Periaux, J.: A fictitious domain approach to the direct numerical simulation of incompressible viscous flow past moving rigid bodies: application to particulate flow. J. Comput. Phys. **169**(2), 363–426 (2001)
23. Gualtieri, P., Picano, F., Sardina, G., Casciola, C.M.: Exact regularized point particle method for multiphase flows in the two-way coupling regime. J. Fluid Mech. **773**, 520–561 (2015)
24. Hartmann, D., Meinke, M., Schröder, W.: A strictly conservative cartesian cut-cell method for compressible viscous flows on adaptive grids. Comput. Meth. Appl. Mech. Eng. **200**(9), 1038–1052 (2011)

25. Horwitz, J., Mani, A.: Accurate calculation of stokes drag for point–particle tracking in two-way coupled flows. J. Comput. Phys. **318**, 85–109 (2016)
26. Ireland, P.J., Desjardins, O.: Improving particle drag predictions in euler–lagrange simulations with two-way coupling. J. Comput. Phys. **338**, 405–430 (2017)
27. Kim, S., Karrila, S.J.: Microhydrodynamics: principles and selected applications. Courier Corporation (2013)
28. Kuerten, J.: Subgrid modeling in particle-laden channel flow. Phys. Fluids **18**(2), 025,108 (2006)
29. Kuerten, J.: Point-particle dns and les of particle-laden turbulent flow-a state-of-the-art review. Flow, Turbulence and Combustion **97**(3), 689–713 (2016)
30. Kuerten, J., Vreman, A.: Can turbophoresis be predicted by large-eddy simulation? Phys. Fluids **17**(1), 011,701–011,701 (2005)
31. van Leer, B.: Towards the ultimate conservative difference scheme. v. a second-order sequel to godunov's method. J. Comput. Phys. **32**(1), 101 – 136 (1979)
32. Liou, M.S., Steffen, C.J.: A new flux splitting scheme. J. Comput. Phys. **107**(1), 23–39 (1993)
33. Lucci, F., Ferrante, A., Elghobashi, S.: Modulation of isotropic turbulence by particles of taylor length-scale size. J. Fluid Mech. **650**, 5–55 (2010)
34. Maxey, M., Patel, B., Chang, E., Wang, L.P.: Simulations of dispersed turbulent multiphase flow. Fluid Dyn. Res. **20**(1), 143 – 156 (1997)
35. Maxey, M.R., Riley, J.J.: Equation of motion for a small rigid sphere in a nonuniform flow. Phys. Fluids **26**(4), 883–889 (1983)
36. Meinke, M., Schröder, W., Krause, E., Rister, T.: A comparison of second-and sixth-order methods for large-eddy simulations. Comput. Fluids **31**(4), 695–718 (2002)
37. Meysonnat, P.S., Roggenkamp, D., Li, W., Roidl, B., Schröder, W.: Experimental and numerical investigation of transversal traveling surface waves for drag reduction. Eur. J. Mech. B / Fluids **55**, 313–323 (2016)
38. Michałek, W., Kuerten, J.G., Zeegers, J., Liew, R., Pozorski, J., Geurts, B.J.: A hybrid stochastic-deconvolution model for large-eddy simulation of particle-laden flow. Phys. Fluids **25**(12), 123,302 (2013)
39. Orszag, S.A.: Numerical methods for the simulation of turbulence. Phys. Fluids **12**(12), II–250 (1969)
40. Pope, S.: Turbulent Flows. Cambridge University Press (2000)
41. Renze, P., Schröder, W., Meinke, M.: Large-eddy simulation of film cooling flows at density gradients. Int. J. Heat Fluid Flow **29**(1), 18–34 (2008)
42. Rütten, F., Schröder, W., Meinke, M.: Large-eddy simulation of low frequency oscillations of the dean vortices in turbulent pipe bend flows. Phys. Fluids **17**(3), 035,107 (2005)
43. Schneiders, L., Günther, C., Meinke, M., Schröder, W.: An efficient conservative cut-cell method for rigid bodies interacting with viscous compressible flows. J. Comput. Phys. **311**, 62–86 (2016)
44. Schneiders, L., Hartmann, D., Meinke, M., Schröder, W.: An accurate moving boundary formulation in cut-cell methods. J. Comput. Phys. **235**, 786–809 (2013)
45. Schneiders, L., Meinke, M., Schröder, W.: Direct particle-fluid simulation of kolmogorov-length-scale size particles in decaying isotropic turbulence. J. Fluid Mech. **819**, 188 – 227 (2017)
46. Schneiders, L., Meinke, M., Schröder, W.: On the accuracy of lagrangian point-mass models for heavy non-spherical particles in isotropic turbulence. Fuel **201**, 2 – 14 (2017)
47. Schumann, U., Patterson, G.: Numerical study of pressure and velocity fluctuations in nearly isotropic turbulence. J. Fluid Mech. **88**(4), 685–709 (1978)
48. Shotorban, B., Mashayek, F.: A stochastic model for particle motion in large-eddy simulation. J. Turbul. **7**, N18 (2006)
49. Squires, K.D., Eaton, J.K.: Particle response and turbulence modification in isotropic turbulence. Phys. Fluids A **2**(7), 1191–1203 (1990)
50. Strutt, H., Tullis, S., Lightstone, M.: Numerical methods for particle-laden dns of homogeneous isotropic turbulence. Computers & Fluids **40**(1), 210–220 (2011)
51. Sundaram, S., Collins, L.R.: Numerical considerations in simulating a turbulent suspension of finite-volume particles. J. Comput. Phys. **124**(2), 337–350 (1996)
52. Thornber, B., Drikakis, D., Williams, R.J., Youngs, D.: On entropy generation and dissipation of kinetic energy in high-resolution shock-capturing schemes. J. Comput. Phys. **227**(10), 4853–4872 (2008)

53. Thornber, B., Mosedale, A., Drikakis, D.: On the implicit large eddy simulations of homogeneous decaying turbulence. J. Comput. Phys. **226**(2), 1902–1929 (2007)
54. Thornber, B., Mosedale, A., Drikakis, D., Youngs, D., Williams, R.J.: An improved reconstruction method for compressible flows with low mach number features. J. Comput. Phys. **227**(10), 4873–4894 (2008)
55. Turkel, E.: Preconditioning techniques in computational fluid dynamics. Annu. Rev. Fluid Mech. **31**(1), 385–416 (1999)
56. Van Atta, C., Antonia, R.: Reynolds number dependence of skewness and flatness factors of turbulent velocity derivatives. Phys. Fluids (1958-1988) **23**(2), 252–257 (1980)
57. Wang, Q., Squires, K.D.: Large eddy simulation of particle-laden turbulent channel flow. Phys. Fluids **8**(5), 1207–1223 (1996)
58. Xu, Y., Subramaniam, S.: Consistent modeling of interphase turbulent kinetic energy transfer in particle-laden turbulent flows. Phys. Fluids **19**(8), 085,101 (2007)
59. Zeng, L., Balachandar, S., Fischer, P., Najjar, F.: Interactions of a stationary finite-sized particle with wall turbulence. J. Fluid Mech. **594**, 271–305 (2008)